CHALMERS
UNIVERSITY OF TECHNOLOGY

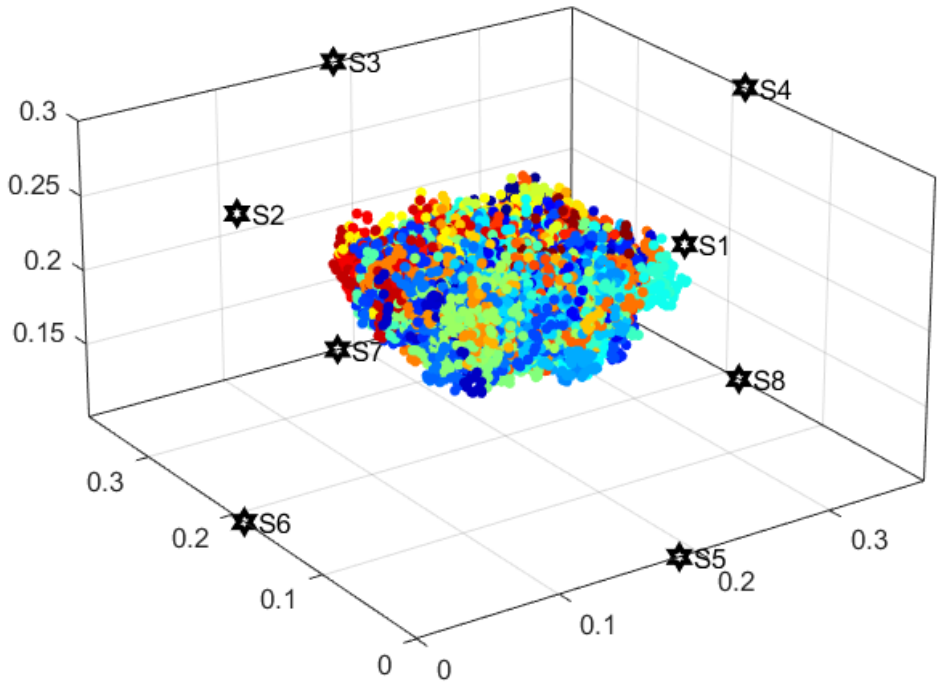

Impact of Gas Release on the Mixing of Large Particles in Bubbling Fluidized Beds

Master's thesis in Sustainable Energy Systems

JING SHI

DEPARTMENT OF SPACE, EARTH AND ENVIRONMENT

CHALMERS UNIVERSITY OF TECHNOLOGY
Gothenburg, Sweden 2024
www.chalmers.se

MASTER'S THESIS 2024

Impact of Gas Release on the Mixing of Large Particles in Bubbling Fluidized Beds

JING SHI

CHALMERS
UNIVERSITY OF TECHNOLOGY

Department of Space, Earth and Environment
Chalmers University of Technology
Gothenburg, Sweden 2024

Impact of Gas Release on the Mixing of Large Particles in Bubbling Fluidized Beds
JING SHI

Supervisor: Diana Carolina Guío-Pérez, Department of Space, Earth and Environment
Examiner: David Pallarès, Department of Space, Earth and Environment

Master's Thesis 2024
Department of Space, Earth and Environment
Chalmers University of Technology
SE-412 96 Gothenburg
Sweden
Telephone +46 31 772 1000

Cover: Trajectory points of high-density gas-releasing tracer in a bubbling fluidized bed with a fluidization number of 5.

Typeset in LaTeX
Printed by Chalmers Reproservice
Gothenburg, Sweden 2024

Impact of Gas Release on the Mixing of Large Particles in Bubbling Fluidized Beds
JING SHI
Department of Space, Earth and Environment
Chalmers University of Technology

Abstract

This study experimentally investigates solids mixing within a bubbling fluidized bed using a fluid-dynamically downscaled cold model and Magnetic Particle Tracking technology. The trajectories of gas-releasing tracers were tracked and compared to blank tracers to analyze the impact of gas release on mixing for various tracer densities and fluidization numbers. Lateral mixing was quantified using Einstein's equation for Brownian motion, and probability density functions was utilized to analyze the axial position and velocity distribution of the tracers.

The results indicate that gas release significantly enhances the lateral mixing of low-density tracers at high fluidization numbers, while it has a more pronounced effect on the mixing of heavy tracers at low fluidization numbers. Additionally, gas release affects the vertical distribution of tracers in a complex manner, depending on the tracer density and fluidization number. Gas-releasing tracers with low density tend to immerse more into the bed at low fluidization numbers, while high-density gas-releasing tracers tend to remain at higher axial positions. The impact of gas release on the velocity of the tracers is significant only at high gas release rates, for which the force balance on the tracers seems to be impacted, causing higher fluctuations in the velocity.

Keywords: Solids mixing, gas release, bubbling fluidized bed, biomass pyrolysis, magnetic particle tracking.

Acknowledgements

I would like to express my deepest gratitude to my supervisor, Carolina, for her invaluable assistance throughout this thesis. She provided me with numerous ideas on how to handle and analyze data, as well as how to proceed with subsequent experiments. Each weekly meeting with her was a learning experience, and her insightful suggestions significantly improved the flow of my thesis.

I am also very thankful to Azka for her extensive help during my experiments. Her contributions to the discussions in our weekly meetings provided me with additional insights. Finally, I would like to thank my examiner, David, for his guidance throughout this entire work.

Jing Shi, Gothenburg, May 2024

Nomenclature

Abbreviations

AMR	Anisotropic magneto-resistive
FN	Fluidization number
MPT	Magnetic particle tracking
PDF	Probability density function
PET	Polyethylene terephthalate
PSD	Particle size distribution

Greek symbols

ρ_g	Gas density	kg/m^3
ρ_p	Particle density	kg/m^3
μ_f	Dynamic viscosity of the flow	Pa·s
Ψ	Sphericity	-

Latin symbols

d_p	Characteristic length of particle	m
D	Characteristic length	m
D_k	Dispersion coefficient along different directions	m^2/s
D_r	Radial dispersion coefficient	m^2/s
g	Gravitational acceleration	m/s^2
Δl_k	Displacement along different directions	m
Δr	Radial displacement	m
Δt	Time	s

u_o	Superficial flow velocity	m/s
u_{mf}	Minimum fluidization velocity	m/s

Contents

List of Figures

List of Tables

1
Introduction

Due to the scarcity of fossil fuel resources and the increasing severity of global warming, the development of technologies for the conversion of renewable and environmentally friendly fuels is urgently needed. Biomass conversion is increasingly gaining attention due to its renewability, biodegradability, and carbon-neutral characteristics [1]. Compared to traditional fossil fuels, biomass releases significantly fewer nitrogen and sulfur oxides during conversion [2]. Additionally, the use of biomass helps reduce methane emissions from landfills, reduces land occupation, and provides a stable energy supply and economic feasibility [3].

Biomass can be converted into different types of energy and valuable streams through various thermochemical conversion processes such as combustion, gasification, and pyrolysis [4]. Although combustion is a common method for obtaining thermal energy and electricity, the emissions and ash waste compromise its environmental friendliness [5]. Gasification provides another efficient way to use biomass, but involves higher storage and transportation costs, and produces tar pollutants [5]. Pyrolysis, a thermal decomposition process carried out in an inert atmosphere, primarily produces non-condensable gases (CO, CO_2, H_2, CH_4, etc.), liquids (bio-oil), and solid (biochar) [6]. Depending on the heating rate, it can be divided into fast and slow pyrolysis. Fast pyrolysis, characterized by its rapid reaction speed, high conversion efficiency, and high energy density of products, demonstrates significant market potential, especially considering the expected shift in biomass utilization from heat and electricity production to the generation of valuable industrial products [7].

The bubbling fluidized bed is widely used in the biomass pyrolysis field due to the simple configuration of the reactors, convenient operation, long service life, and high adaptability to biomass particles [4]. Usually, the addition of inert bulk solids (such as quartz sand, ceramic balls, high alumina bauxite, etc.) improves the fluid dynamics, therefore making the conversion of biomass particles with typically poor flowability more effective and preventing agglomeration [6]. Compared to bulk solids, biomass particles are generally larger and lighter, and their mass usually makes up only a small fraction of the total mass of solids in the fluidized bed [8]. The intense mixing of bulk solids with biomass particles not only provides a uniform temperature distribution but also enhances mass and heat transfer [6].

Due to the density and size differences between biomass particles and bulk solids, axial segregation is likely to occur, leading to uneven biomass concentration along the bed height [9]. Biomass on the surface of the fluidized bed differs significantly in the heat and mass transfer it is subjected to compared to biomass within the

bed. Surface biomass experiences stronger mass transfer and weaker heat transfer, leading to faster char conversion as well as slower drying and devolatilization [10]. Insufficient lateral mixing can also lead to uneven distribution of volatiles and char products [11]. This insufficient mixing affects the uniformity of the temperature field within the fluidized bed, potentially leading to the formation of hot and cold spots and reducing the efficiency and stability of the reactor, and affecting the quality of the products [12]. Therefore, a comprehensive understanding of the mixing process is crucial for optimizing heat distribution and product quality.

Besides, volatile gases are released during the devolatilization and drying of biomass, which are suspected to evolve as endogenous bubbles, further affecting the mixing of the material [9][13]. Iannello used X-ray imaging technology to observe the devolatilization behavior of individual raw material particles at high temperatures, finding that volatiles exist in the form of endogenous bubbles, providing lift to the particles that often drags them to the surface of the bed [9]. Solimene's research indicates that the lifting force produced by volatile gases depends on the flow rate of the emitted gas and the size of the particles, rather than the superficial speed of the fluidizing gas [13]. However, these studies only focused on the influence of endogenous bubbles when the fluidization number (FN), which is the ratio of the superficial gas velocity to the minimum fluidization velocity (u_{mf}), is between 1 and 2, and the particle is immersed in the bed. The minimum fluidization velocity is the velocity at which the drag force from the fluid equals the weight of the particles, causing them to become suspended. Given the wide variation in FNs in actual industrial applications, further experiments are needed to explore the impact of gas release under different FNs on solids mixing. Moreover, studies on the mixing behavior of large particles of different densities during fluidization are still scarce [14].

This study aims to explore how gas release affects the mixing behavior of large particles within a bubbling fluidized bed under different FNs and for different particle densities. The experiment used a fluid-dynamically downscaled cold model to simulate the operation of fluidized beds in industrial biomass conversion applications. The high-resolution trajectory of individual gas-releasing tracers within the fluidized bed was tracked using Magnetic Particle Tracking (MPT) technology.

2
Theory

This section briefly introduces the principles behind pyrolysis, fluidization, solids mixing and segregation, lateral dispersion coefficient, as well as fluid dynamic scaling laws.

2.1 Biomass pyrolysis

Pyrolysis is a process of heating organic materials under oxygen-deficient conditions to convert them into biochar, condensable liquid bio-oil, and non-condensable gases. The products not only have a high energy density but can also be further processed to yield higher-value biofuels or other chemicals [6]. This important biomass thermochemical conversion process is also a precursor step to char gasification and combustion [6].

The industrial process for pyrolysis involves three key stages: the initial stage includes the collection, storage, and preprocessing of raw materials; followed by the thermochemical conversion stage, where the biomass first undergoes moisture evaporation and initial decomposition reactions, followed by more complex secondary reactions, such as cracking and reformation; the final stage involves upgrading the products using chemical or physical methods to meet marketable standards [15]. These steps collectively constitute a complete process of converting biomass into various useful energy products. The efficiency of pyrolysis and the quality of the final products are influenced by several factors, including the type, size, and moisture content of the feedstock, the pretreatment methods, the specific conditions of the reaction (such as residence time, pressure, temperature, and heating rate), and the design and selection of the reactor [16].

The thermochemical conversion of biomass is a complex process involving multiple steps and different temperature ranges [15][17][18]. Initially, free water in the biomass is removed by evaporation, followed by the primary decomposition stage, which includes char formation, depolymerization of polymer units, and the fragmentation of internal bonds within monomer units [17]. During depolymerization, the degree of polymerization of the polymer chains decreases, producing volatile substances, which are typically collected and converted into liquid fractions. The fragmentation process generates non-condensable gases and linear compounds [18]. Subsequently, under the high temperatures in the reactor, the less stable volatile compounds may trigger a series of secondary reactions. These reactions primarily involve cracking and recombination, occurring both in the gas phase and between

the gas and solid phases. Volatile compounds may undergo cracking due to chemical bond breakage to form lighter molecules, or they may recombine to form heavier molecules [18]. Additional solid carbon is formed as these compounds recombine in the pores of the solid product [18]. Different biomass components decompose at different temperature ranges due to their varying thermal stability. Hemicellulose decomposes quickly within the 220-315°C range, cellulose starts decomposing at 315-400°C, and lignin decomposes slowly and continuously over a broader temperature range of 160-900°C [15].

In the pyrolysis products, pyrolysis oil contains 15-35% water and hundreds of organic components, including acids, alcohols, ketones, aldehydes. Biochar contains unconverted organic materials and carbonaceous residues along with the majority of mineral compounds. The pyrolysis process also releases a variety of gases, such as carbon dioxide, carbon monoxide, hydrogen, various low-carbon hydrocarbons, and a small number of other gases, such as ammonia and sulfur oxides [19].

2.2 Fluidization technology and its application in biomass pyrolysis

Fluidization refers to the suspension of fine solid particles in a gas or liquid fluid flow, allowing them to exhibit a fluid-like behavior [21]. Fluidization occurs due to the upward drag of the fluid against the solid particles. When the fluid ascends at a slow pace, it primarily flows through the narrow spaces between the particles, resulting in a pressure drop but unable to move the solid particles. This is known as a fixed bed. As the fluid velocity increases, fluid drag also increases, causing the bed layer to expand. This process continues until the fluid velocity reaches a critical point, the minimum fluidization velocity. At this point, the upward force of the fluid equals the weight of the particles, transforming the fixed bed into a fluidized bed. Further increase of the fluid flow rate leads to the onset of different fluidization regimes, such as bubbling regime, slugging regime, and turbulent regime (as shown in Figure 2.1) [20][21]. The main characteristics of the most commonly referred fluidization regimes are mentioned below. The onset and the use of these different regimes depend on the characteristics of the reactor and the fluid and solids phases involved.

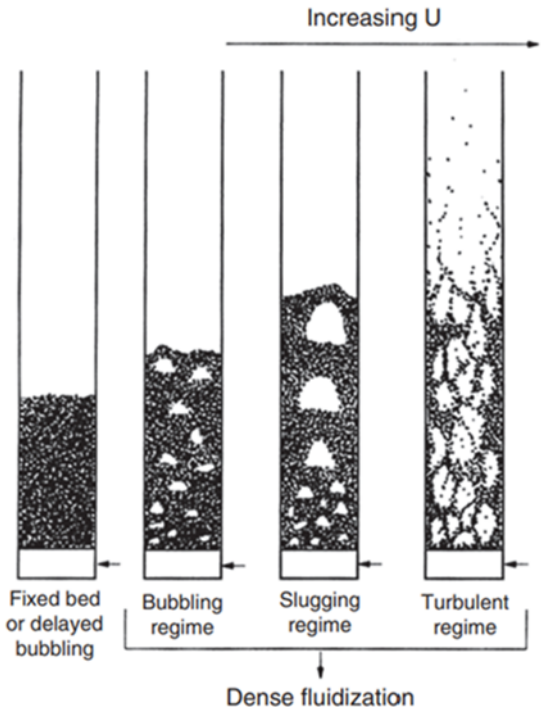

Figure 2.1: Fluidization patterns in gas-solid systems, modified from [21].

In gas-fluidized beds, when the velocity of the gas exceeds the minimum fluidization velocity of the particles, significant instability is observed in the bed layer. This instability typically accompanies the formation of bubbles. Excess gas traverses the bed in the form of bubbles. Bubbles are regions with low solid density, while regions with higher solid density are referred to as the emulsion phase or dense phase. Initially, small bubbles form at the distributor, and as they ascend through the bed, they grow, coalesce, and split. The characteristics of bubbles, such as their diameter and frequency within the reactor largely determine the fluid dynamics of the bed. In turn, these characteristics are significantly influenced by the types and sizes of the solids present, as well as the properties of the gas.

Geldart classified solids into four distinct groups: Group A, B, C, and D [22]. The solids used in this study belong to Group B, which includes sand-like particles with sizes ranging from 40 μm to 500 μm and densities between 1.4 g/cm^3 and 4 g/cm^3, approximately. For Group B solids, the bubble size grows approximately linearly with the distance from the distributor and with the gas velocity. The frequency of bubbles is also associated with the excess gas flow rate, defined as the difference between the superficial gas velocity and the minimum fluidization velocity. At increased flow rates, gas can also establish continuous pathways between solids, referred to as gas channels. These channels enable the gas to traverse the bed layer more rapidly, intensifying the agitation of the particles.

In small-diameter fluidized beds, bubbles absorb more gas as they move upward through the bed layer. As gas continues to be supplied, the volume of the bubbles gradually increases. They may eventually cover the entire cross-section of the container. Fine particles can slide along the container's walls in the gaps formed by the

rising gas flow, which is known as slug fluidization. Slugs continuously disintegrate and regenerate, causing unstable oscillating motion.

When the gas velocity becomes sufficiently high, the top interface of the fluidized bed disappears, and particles start being significantly carried by the airflow. Within the bed, clusters of solid particles of different sizes and shapes exhibit intense turbulent motion. This behavior signifies the transition of the fluidized bed from a dense phase to a dilute-phase state. To mitigate particle loss, cyclone separators can be utilized to capture the carried particles and recirculate them back into the bed.

The core function of a biomass pyrolysis reactor is to ensure that the inputted biomass is uniformly and fully heated and converted. This is linked to the achievement of the required temperature and specific effective residence time[15]. Particularly in the fast pyrolysis process, the reactor must be designed to transfer a substantial amount of heat to the biomass rapidly, while also minimizing the residence time of the fluidization medium within the reactor [17]. The method of mixing biomass particles with preheated heat carriers (such as sand) is widely used [6]. Bubbling fluidization technology, known for its straightforward structure and simple operation, is widely used to enhance heat and mass mixing between the heat carrier and biomass. This intense mixing ensures a uniform temperature distribution and effective heat transfer, thereby improving the efficiency and quality of the pyrolysis process [15].

2.3 Solids mixing and segregation

The mixing of solid particles in fluidized beds manifests in two directions: lateral and axial [23]. Lateral mixing is primarily caused by the lateral diffusion of particles entering from the feed inlet. Axial mixing is driven by differences in particle size and density, with lighter or finer particles rising to the top of the bed and heavier or coarser particles settling at the bottom. The agitation of solids by gas bubbles also significantly influences the mixing of different solid phases within the bed.

In a bubbling bed, bubbles can generally be categorized into two types [9]. The first type consists of exogenous bubbles, which originate from the fluidizing gas (as described above). The second type comprises endogenous bubbles, which are formed from gases released by particles due to thermochemical reactions.

Exogenous bubbles serve as the primary driving force for solids mixing in fluidized beds [23]. This mixing is primarily achieved through three mechanisms: first, solid particles experience lateral displacement caused by bubble eruptions at the bed surface; second, a lifting effect occurs in the wake of ascending bubbles, drawing solid particles upwards; and third, the emulsion phase sinks, with particles outside the bubble regions moving downward to fill the spaces left by the rising bubbles [20]. These sinking particles are recaptured by the wake at the bed bottom and ejected upwards, undergoing horizontal displacement before sinking back into the dense bed, thus forming a continuous mixing cycle [24].

In a two-dimensional experiment, Pallarès observed that solid mixing manifested as horizontally arranged vortices with alternating rotational directions [24]. These vortex structures and the surrounding local flow structures can be divided into different mixing cells [25]. During the sinking of the emulsion drift, solid exchanges also occur between adjacent cells [25].

Some researchers found that the formation of endogenous bubbles is related to the release of volatile gas [26]. Exogenous bubbles contribute to improved mixing of solids. In contrast, endogenous bubbles can cause segregation along the vertical axis, leading to stratification throughout the bed height and resulting in ineffective solids mixing [26]. Iannello et al. observed the evolution and detachment of endogenous bubbles using X-ray imaging technology [9]. And they found that higher release rates produce larger bubbles, which provide greater buoyancy to the reactive fuel. Solimene et al. revealed that gas emissions promote momentum exchange between the bed solids and gas-emitting particles, thereby increasing their buoyancy [13]. The magnitude of this buoyancy depends on the particle size and the gas release rate.

2.4 Lateral dispersion coefficient

The radial dispersion coefficient is one of the methods used to quantify the lateral mixing of solids within a fluidized bed [25]. It can be calculated using Einstein's equation for Brownian motion, as shown in Equation 2.1 [29].

$$D_r = \frac{1}{2}\frac{(\Delta r)^2}{\Delta t} \tag{2.1}$$

where Δr represents radial displacement and Δt is the time interval between the initial and final positions. However, lateral mixing usually exhibits a certain degree of anisotropy [11]. Therefore, it is a common practice to analyze the lateral mixing in each of the two directions x and y separately, as it is displayed in Equation 2.2 [11].

$$D_k = \frac{1}{2}\frac{(\Delta l_k)^2}{\Delta t} \qquad k = x, y \tag{2.2}$$

where Δl_k is the net displacement along the x or y axis. It is worth mentioning that in large units featuring nozzles that are evenly spaced, it is reasonable to assume that solids mixing remains uniform and consistent across both lateral directions [11]. This implies isotropic solids mixing, thereby enabling the application of a single dispersion coefficient for the analysis ($D_x = D_y$). The relationship between D_r and D_k is shown in Equation 2.3.

$$D_r^2 = D_x^2 + D_y^2 \tag{2.3}$$

2.5 Fluid-dynamically scaling

In commercial applications, fluidized beds often have very large diameters and heights and operate at very high temperatures. Under such conditions, collecting data and designing tests can be extremely difficult. The resolution of the extracted data and the quality of the information is very limited [27]. Therefore, scaling relationships are commonly used to simulate the fluid dynamics of large reactors while working at room temperature and ambient pressure in small units, so called cold flow models. These scaling relationships not only maintain fluid dynamic similarity but also make operations simpler, more flexible, and cost-efficient. Additionally, they allow for the use of more precise diagnostic tools [27]. Currently, the scaling laws developed by Glicksman are the most widely used and validated [28]. According to the principles of mass and momentum conservation for both fluids and particles, the dimensionless scaling parameters shown in Table 2.1 ensure similar fluidization conditions across reactors of different scales.

Table 2.1: Dimensionless numbers and their definitions in Glicksman's full scaling laws

Dimensionless number	**Expression**	**Definition**
Froude number	$\frac{{u_0}^2}{gD}$	The ratio of inertial forces to gravitational forces
Density ratio	$\frac{\rho_p}{\rho_f}$	The ratio of particle density to fluid density
Particle Reynolds number	$\frac{\rho_p u_0 d_p}{\mu_f}$	The ratio of particle inertial forces to viscous forces
Fluid Reynolds number	$\frac{\rho_f u_0 L}{\mu_f}$	The ratio of fluid inertial forces to viscous forces
Aspect ratio	$\frac{L}{D}$	The ratio of length to diameter
Sphericity	Ψ, PSD	The distribution and sphericity of particles
Circulation rate	$\frac{G_s}{\rho_p u_0}$	Solids circulation rate

By combining the Froude number and the Reynolds number, the length scaling factor in Equation 2.4 can be obtained. However, the value only depends on the gas used, which limits the choice of cold models.

$$[L] = \frac{D_{\text{cold}}}{D_{\text{hot}}} = \left(\frac{\frac{\rho_f}{\mu_f}|_{\text{cold}}}{\frac{\rho_f}{\mu_f}|_{\text{hot}}} \right)^{2/3} \tag{2.4}$$

3
Methods

This section briefly introduces the experimental setup from the perspectives of tracer, cold model, and Magnetic Particle Tracking technology, and covers the experimental procedures, test matrix, and data processing methods.

3.1 Experimental setup

3.1.1 Tracers and simulation of gas release

The foundation of the experiment is to track the movement of a single cylindrical-shaped tracer (schematically shown in Figure 3.1) within a bubbling fluidized bed. To simulate the gas release during the drying and devolatilization processes of biomass, both ends of the cylindrical shell are filled with dry ice pellets (distributed as evenly as possible). Prior to the filling procedure, a cylindrical magnet with a diameter and length of 3 mm is fixed in the center of the shell to enable trajectory tracking using Magnetic Particle Tracking technology, which will be introduced in Section 3.1.3. The interior of the shell is threaded, allowing it to be sealed at both ends with caps. The caps are formed by a threaded body and a porous polyester material in the center to ensure effective gas release.

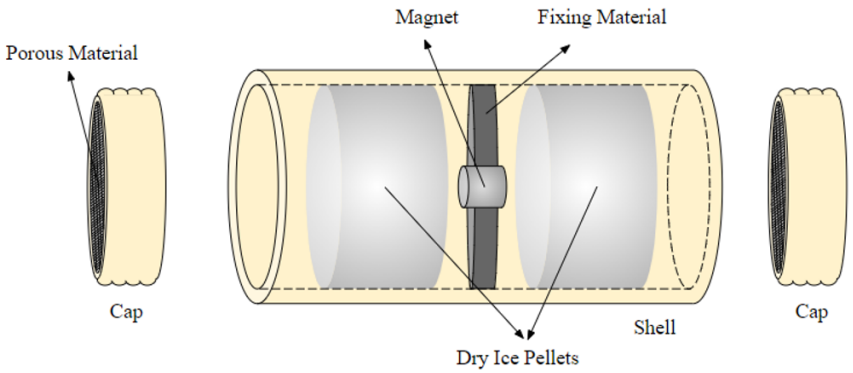

Figure 3.1: Structural schematic diagram of tracers.

Since biomass particles are larger and lighter than bed material particles, shells made of Polyethylene Terephthalate (PET), which has a lower density, are used for the experiment to meet fluid-dynamically scaling requirements. Such light particles, due to their low density, tend to float on the bed surface during low fluidization velocity,

limiting the extend of possible behaviors to be observed. Consequently, experiments also employ shells fabricated from bronze (about 2.5 times heavier than PET). The minor differences in size between the two shell types are considered negligible. To better compare with the gas-releasing tracer, experiments are also conducted with the tracer without filling dry ice (blank tracer). The density of the low-density tracer (PET shell) changes by 14% before and after filling with dry ice, and the density of the high-density tracer (bronze shell) changes by 4%, indicating a relatively smaller density change. Detailed properties of the tracers used are provided in Table 3.1.

Table 3.1: Properties of the tracers used.

Shell material	**Diameter [mm]**	**Length [mm]**	**Density (without dry ice)) [kg/m^3]**	**Density (with dry ice) [kg/m^3]**
PET	17.5	12	1791	2045
Bronze	16	13	5181	5432

3.1.2 Fluid-dynamically downscaled cold model

In this study, experiments were conducted in a fluid-dynamically downscaled bubbling fluidized bed with a cross-section area of 0.17 × 0.17 m^2 and a height of 0.18 m to simulate typical conditions for the thermochemical conversion of biomass. According to Glicksman's scaling laws, this cold model corresponds to a fluidized bed reactor operating at 700 °C with a cross-section of 0.71 × 0.71 m^2 and a height of 0.16 m. A schematic of the cold model is shown in Figure 3.2.

At room temperature, pressurized air uniformly enters the bed through a porous plate from the bottom to achieve a homogeneous bubbling fluidization state. The bed material consists of bronze powder with a static bed height of 4.5 cm, an average particle size of 189 microns, and a particle density of 8492 kg/m^3. The theoretical minimum fluidization velocity is 0.09 m/s, while the actual minimum fluidization velocity was empirically determined to be 0.083 m/s by gradually increasing the airflow until a ruler could be easily inserted into the fluidized bed, at which point the airflow rate was defined as the minimum fluidization velocity.

To verify whether the use of dry ice affects the fluidization state through temperature changes, a thermocouple located in the corner of the fluidized bed recorded temperature variations during the experiment. Gas was sampled from the outlet gas stream using a gas measurement probe at a frequency of 1 Hz to determine the carbon dioxide concentration and calculate the tracer gas release rate. The pipe for the gas outlet is partially filled with aluminum packing material to ensure a thorough mixing of carbon dioxide in the outlet gas stream at the probe sampling point, thus eliminating local measurement biases. The tracer particle was vertically introduced into the bed through an opening at the center of the top plate of the fluidized bed. Key scaling parameters for the tested operating conditions as well as the physical properties of the gas and solids are listed in Table 3.2.

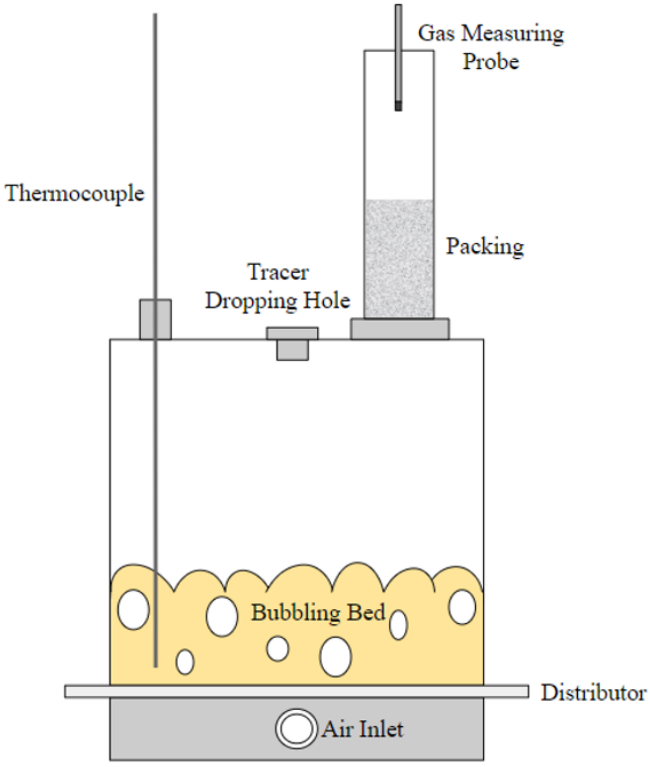

Figure 3.2: Schematic diagram of fluid-dynamically downscaled cold model.

Table 3.2: Scaling of operational conditions and gas and solids properties.

Parameters	**Units**	**Hot model**	**Cold model**
Temperature	°C	700	20
Pressure	atm	1	1
Minimum fluidization velocity	m/s	0.17	0.083
Fluidizing gas density	kg/m^3	0.36	1.2
Bed material size	μm	789	189
Bed material density	kg/m^3	2600	8492
Biomass size	mm	0.01 - 90	0.0026 - 23.76
Biomass density	kg/m^3	50 - 700	165 - 2300

3.1.3 Magnetic Particle Tracking technology

Magnetic Particle Tracking (MPT) technology was employed to acquire precise trajectories of tracer particles with high spatial and temporal resolution. This technique utilizes anisotropic magneto-resistive (AMR) sensors to measure changes in

the magnetic field within the fluidized bed. When the magnetic field interacts with these sensors, the magneto-resistive effect induces variations in the resistance of the sensor elements, allowing for the determination of the tracer's position and orientation. The magnetic fields mainly come from cylindrical NdFeB permanent magnets, each with a diameter and height of 3 mm, embedded within the tracer shell. To comprehensively capture magnetic field information, eight magneto-resistive sensors were uniformly mounted near the center of each vertical sidewall of the fluidized bed using a frame. The sensors were arranged in two layers on each side, with four sensors per layer distributed on the same horizontal plane (as illustrated in Figure 3.3). These sensors were connected in series and integrated with a data acquisition system configured to a sampling frequency of 100 Hz. The spatial accuracy achieved is 1 mm.

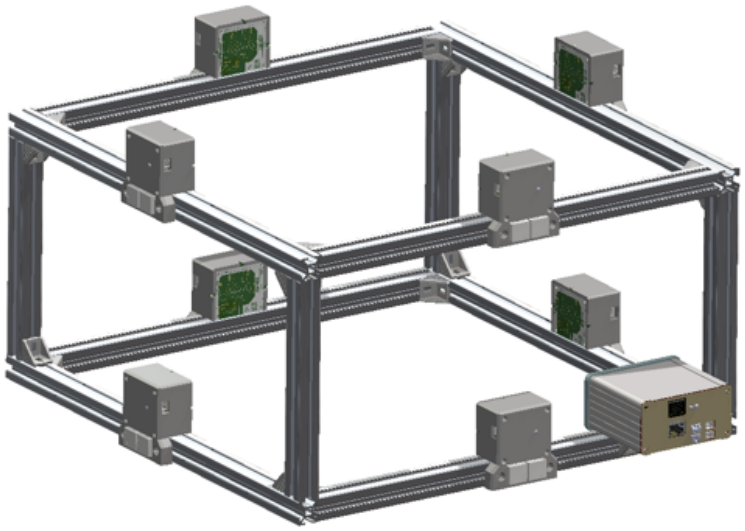

Figure 3.3: Placement of MPT sensors.

3.2 Experimental test matrix

This study investigates the effects of two parameters thought to be strongly linked to the impact of gas release on the mixing dynamic of large particles (such as biomass). These parameters are the density of the large particle and fluidization number (FN). The different particle densities are achieved by utilizing tracer shells made from materials with significantly different densities, specifically PET and bronze. Blank tracers are tested for comparative purposes. To observe the impact of increased fluidization on particle behavior within the bed, experiments were conducted at four different FNs: 1.5, 2, 3.5, and 5. Table 3.3 presents the detailed test matrix.

Table 3.3: Test matrix.

Variables	**Units**	**Values**			
Bed height	m	0.045			
Tracer density	kg/m^3	2045 (PET shell)		5432 (Bronze shell)	
Tracer type	-	Blank		Gas-releasing	
Fluidization number	-	1.5	2	3.5	5

Each experiment with gas-releasing tracers involved tracking the trajectories and measuring the concentration of carbon dioxide until the tracer was depleted, typically lasting about 15 minutes. To ensure the statistical robustness of the data, each set of experimental conditions was replicated five times. As a control, the trajectories of the blank tracer (without filling with dry ice) were also tracked for a duration of 60 minutes.

Before conducting experiments at lower FNs, the fluidized bed was operated at a high fluidization velocity for two minutes to ensure uniform distribution of the fluidizing gas. Due to the use of dry ice, a suction pump was employed to ensure the removal of exhaust gases from the outlet of the fluidized bed, preventing local accumulation of carbon dioxide. Moreover, maintaining the stability of the surrounding magnetic field was crucial for prolonged measurements with MPT sensors. In the absence of the tracer particle, the background magnetic field was measured before each experiment. The background was later removed from the acquired signals to minimize the influence of noise and external magnetic fields on the results. Similarly, background measurements of carbon dioxide concentration were conducted before introducing tracer particles. Only the concentration of carbon dioxide exceeding the ambient concentration was later used. The temperature of the fluidized bed was continuously monitored during the experiment using a thermocouple.

3.3 Data analysis

All trajectory data were processed using MATLAB. The boundaries of the trajectories were determined based on the dimensions of the reactor, and any data points falling outside these boundaries were considered outliers and therefore removed. Since no other variables were altered during the five replicate experiments of each operational condition, the data from these replicates were combined and processed together to enhance statistical robustness. In each experiment, the temperature variation within the fluidized bed was minimal (as illustrated in Figure A.1). Therefore, it can be inferred that the presence of dry ice does not significantly impact the fluid dynamics by altering the temperature field. The following section details the specific computational methods employed.

3.3.1 Lateral dispersion coefficient

To simplify the calculations, this report assumes isotropic solids mixing. First, D_r is calculated through Equation 2.1, and then values for D_x and D_y are obtained using Equation 3.1.

$$D_x = D_y = \frac{D_r}{\sqrt{2}} \tag{3.1}$$

Two aspects are very important when calculating the radial dispersion coefficient. First, the influence of the reactor wall must be eliminated [30]. Thus, when trajectory points are widely distributed across the fluidized bed cross-section, points within 1 cm of the wall are excluded to avoid wall effects. Additionally, it is necessary to ensure that the calculation reflects macroscopic diffusion rather than microscopic movements caused by vibrations [30]. Therefore, a characteristic length scale is chosen as the threshold value. The calculation of the dispersion coefficient is visualized in Figure 3.4.

The position of the tracer at point A is taken as the reference or initial position. A circle is drawn with this point as the center and the threshold value as the radius. Movements of the tracer within this circle are considered microscopic and are not included in the calculation. When the tracer reaches position B, the distance from the current position to the reference position exceeds the threshold length. This distance is then considered an effective displacement for the calculation, and position B is updated as the new reference position.

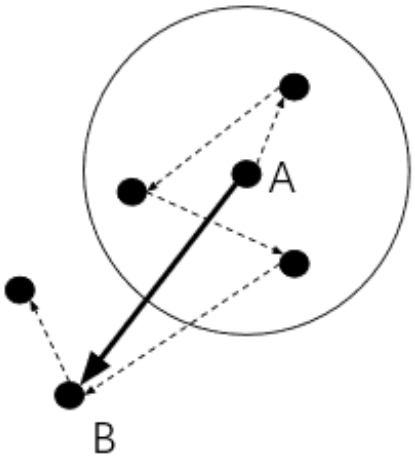

Figure 3.4: Demonstration of effective displacement.

3.3.2 Probability density function

The Probability Density Function (PDF) is used to describe the likelihood of a random variable falling within a specific range of values. This probability is represented by the area under the density curve between two points on the horizontal axis. PDFs

are instrumental in visualizing results, as they highlight significant differences in distributions across various regions. To analyze these distributions, PDFs of different experiments can be plotted on the same graph to examine similarities and differences in their shapes, centers, spreads, and tails.

3.3.3 The combination of trajectories and gas-releasing rate

For the gas-releasing tracer, both the trajectory of the tracer and the concentration of carbon dioxide at the outlet were recorded simultaneously. The trajectory data were processed at 20 Hz to save computational time, whereas the carbon dioxide concentration data were sampled at 1 Hz. Each trajectory point can be associated with a corresponding carbon dioxide release rate. Additionally, due to the distance between the gas measurement probe and the gas analyzer, the measurement features a time lag of about 30 seconds. The gas measurements were corrected accordingly to ensure synchrony between the tracer trajectory and the carbon dioxide concentrations.

The gas release rates were then categorized into different bins according to their magnitudes. Within each bin, the average position of the tracer and its velocity were computed, along with their standard deviations. This allows for an analysis of how the magnitude of the release rate affects these parameters. It is important to note that bins for low release rates contain thousands of data points, whereas bins for high release rates only contain 20-100 data points.

4

Results

The discussion of the results is divided into three parts: lateral mixing, axial mixing, and velocity. Since tracers with different densities exhibit distinct behaviors, the results are presented separately. Additionally, the impact of the fluidization number is presented.

4.1 Lateral mixing

4.1.1 Low-density particle

For low fluidization velocities (FN ≤ 2), both the blank tracer and the gas-releasing tracer with low density always float on the bed surface. They also have a tendency to remain in the corners. The difference between FNs 1.5 and 2 is notable: at FN = 1.5, the tracers move slowly, taking several minutes to reach the corners, whereas at FN = 2, they take only a few seconds. During these experiments, the tracers remain in the same horizontal orientation, constantly colliding with the walls. This results in very small lateral dispersion and a strong influence from the walls, making comparisons difficult and less relevant. These results are not presented here. However, at higher fluidization velocities (FN ≥ 3.5), the tracers exhibit significant lateral dispersion, with their trajectories covering almost the entire horizontal cross-section of the fluidized bed.

Figure 4.1 clearly illustrates the differences in horizontal trajectory distribution between the two tracers (gas-releasing tracer and blank tracer) under higher fluidization conditions. At FNs of 3.5 and 5, high-density regions are evident in the peripheral areas of the fluidized bed, particularly in the lower right corner. The central region of the fluidized bed shows a relatively sparse distribution of data points, without any high-density concentrations. Notably, at a FN of 3.5, the tracers primarily move near the walls. As the FN increases to 5, the higher fluidization velocity causes greater disturbances in the bed, dispersing the tracers towards the central region of the bed and indicating better lateral mixing.

Furthermore, at FN = 3.5, the trajectory differences between the blank tracer and the gas-releasing tracer are minimal. However, when the FN increases to 5, the particle distribution becomes significantly more dispersed, with more trajectory points and a more uniform distribution in the central region of the fluidized bed. This indicates that gas release enhances lateral dispersion. It can be further investigated by calculating the lateral dispersion coefficient.

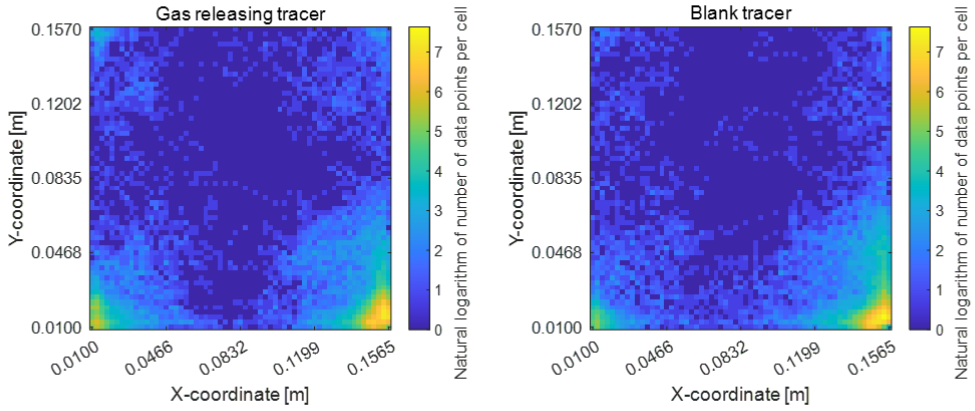

(a) FN = 3.5, a total of 34990 points

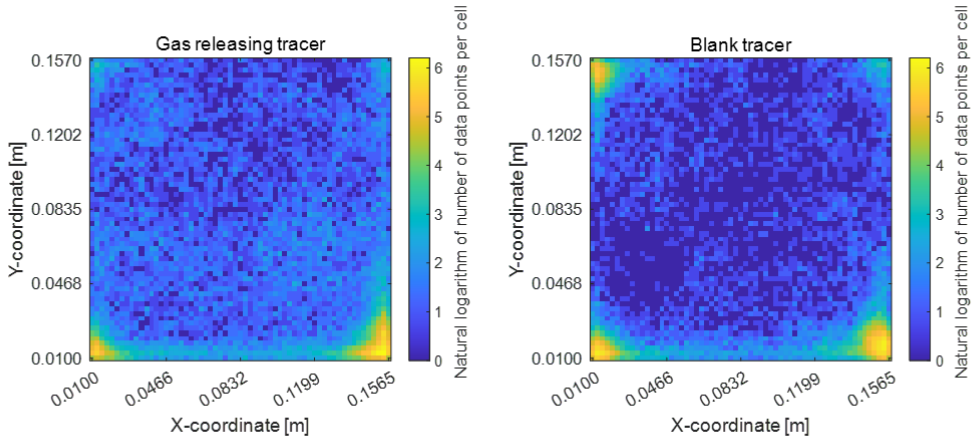

(b) FN = 5, a total of 22519 points

Figure 4.1: Comparison of the total number of trajectory points for low-density gas-releasing tracer and blank tracer within each cell when the fluidized bed is divided into small cells under different fluidization numbers.

As discussed in Section 3.3.1, estimating the macroscopic correlation dispersion coefficient requires selecting a threshold value as the characteristic length scale. Figure 4.2 illustrates the impact of various threshold lengths on the dispersion coefficient D_x and D_y. For a FN of 3.5, the variation in coefficients is minimal, with a dispersion coefficient of $0.4 \times 10^{-3}\ m^2/s$, which aligns with the fact that both the tracers do not move far from the corners. However, for a FN of 5, the dispersion coefficient of the gas-releasing tracer is $1.4 \times 10^{-3}\ m^2/s$, which is significantly greater than that of the blank tracer and is consistent with previous analyses.

Additionally, as the threshold value increases, the dispersion coefficient also in-

creases. This trend is attributed to the reduction in interference caused by microscopic movements and vibrations. A relatively stable value is reached at the threshold of about 0.03 m. Nevertheless, a further increase in the threshold value eventually leads to a decrease in the dispersion coefficient. This phenomenon may occur because the experimental unit size is relatively small so larger thresholds may include trajectories influenced by interaction with the walls. Also, an excessively large threshold value results in too few effective trajectory points, leading to poorer statistical accuracy.

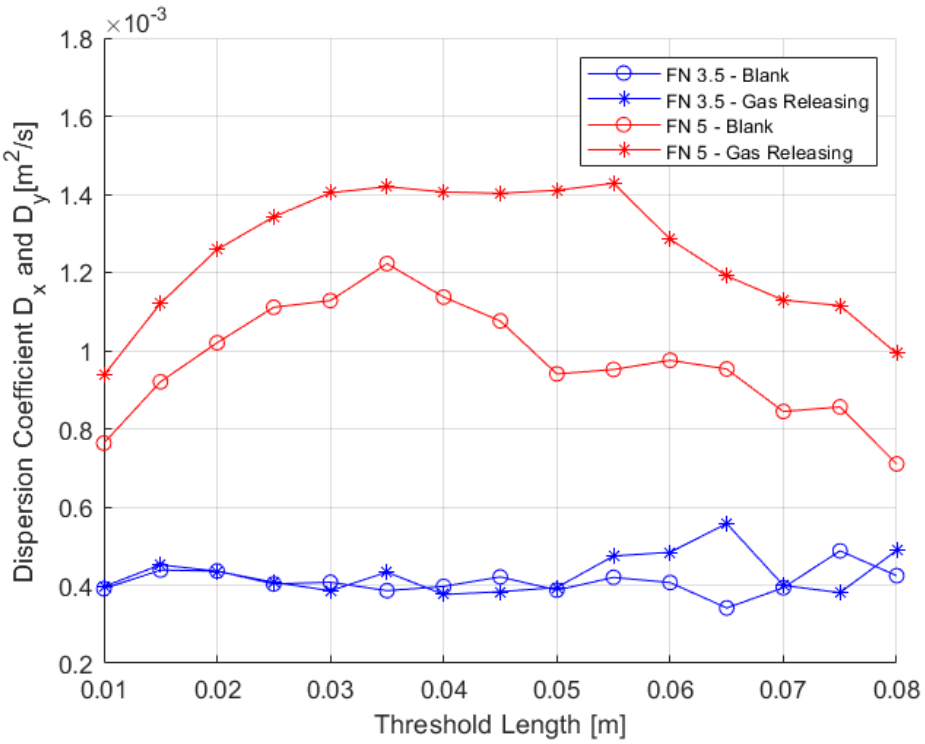

Figure 4.2: Impact of threshold length on dispersion coefficients of low-density tracers at FNs of 3.5 and 5.

4.1.2 High-density particle

The movement of the high-density tracer exhibits significant differences with varying FNs. At a FN of 1.5, similar to the low-density tracer, the high-density tracer slowly moves from the drop point to the corner of the fluidized bed and remains near the corner. When the FN is 2, the tracer initially moves within a small area but eventually becomes trapped in the corners. Thus, the impact of the wall remains significant, and dispersion is therefore not discussed at this stage. With further increases in fluidization velocity, the lateral dispersion of the high-density tracer significantly enhances, and its movement trajectory gradually covers the entire horizontal cross-section of the bed.

Figure 4.3 shows the density map of tracer positions of two types of high-density tracers at FNs of 3.5 and 5. The trajectory distribution of the tracer is relatively

uniform, with data points primarily concentrated in the central region of the fluidized bed, but also present in some peripheral regions. This distribution is in stark contrast to that of the low-density tracer. It is hypothesized that the low-density tracer is more easily pushed by the erupting bubbles to the boundaries. In contrast, the high-density tracer with a density similar to the bed material behaves more like the bulk material and mixes better in the central region. Visual observation clearly shows that the high-density tracers are more likely to remain immersed, suggesting that the mechanisms for lateral movement may differ from those affecting the low-density tracers. Analyzing the axial mixing may provide further insights into this matter. Increasing the fluidization velocity results in a more even distribution of trajectory points of tracers. However, the enhancement of dispersion due to gas release is noticeable only when FN is 3.5.

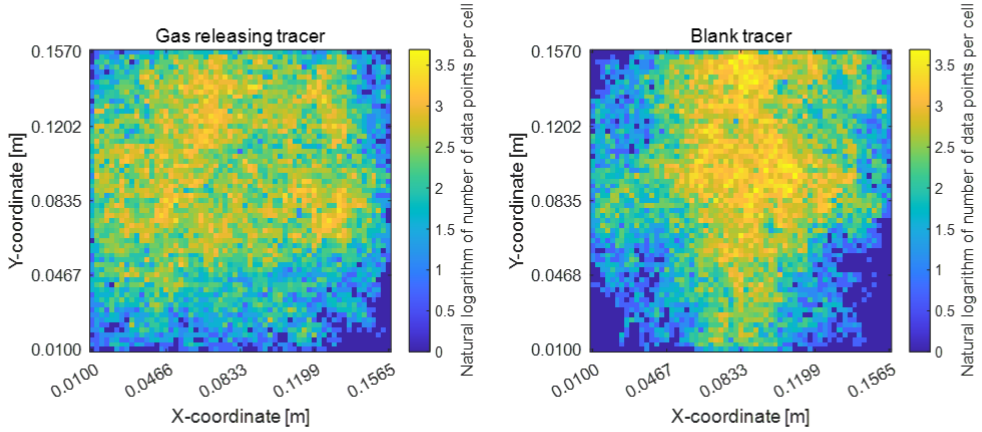

(a) FN = 3.5, a total of 33384 points

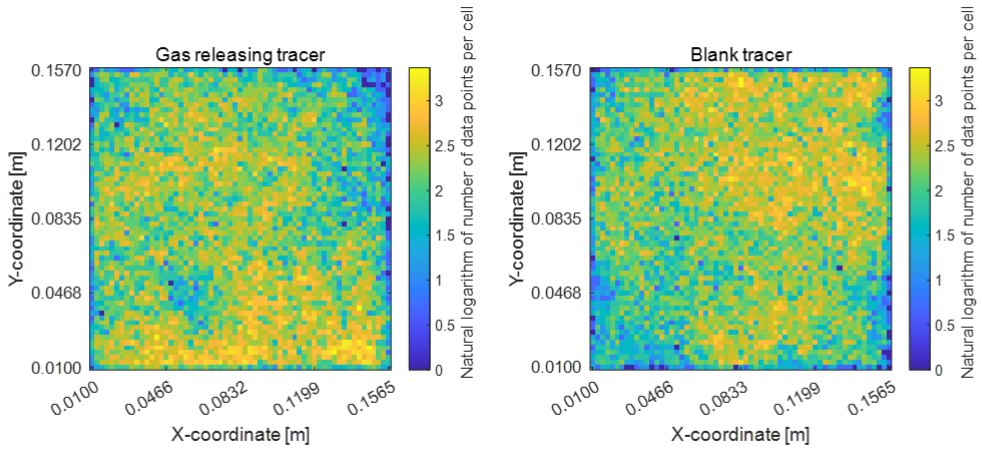

(b) FN = 5, a total of 32022 points

Figure 4.3: Comparison of the total number of trajectory points for high-density gas-releasing tracer and blank tracer within each cell when the fluidized bed is divided into small cells under different fluidization numbers.

The enhancement effect of gas release on lateral mixing at FN = 3.5 is further confirmed by the calculated lateral dispersion coefficient (as shown in Figure 4.4). The dispersion coefficient of the gas-releasing tracer at FN = 3.5 is approximately $0.65 \times 10^{-3}\ m^2/s$, which is about $0.15 \times 10^{-3}\ m^2/s$ higher than that of the blank tracer. However, when the FN is increased to 5, the blank tracer exhibits a higher dispersion coefficient, necessitating further investigation. It must also be noted that the analysis presented here includes the full trajectory of the gas-releasing tracers, encompassing a range of different release rates.

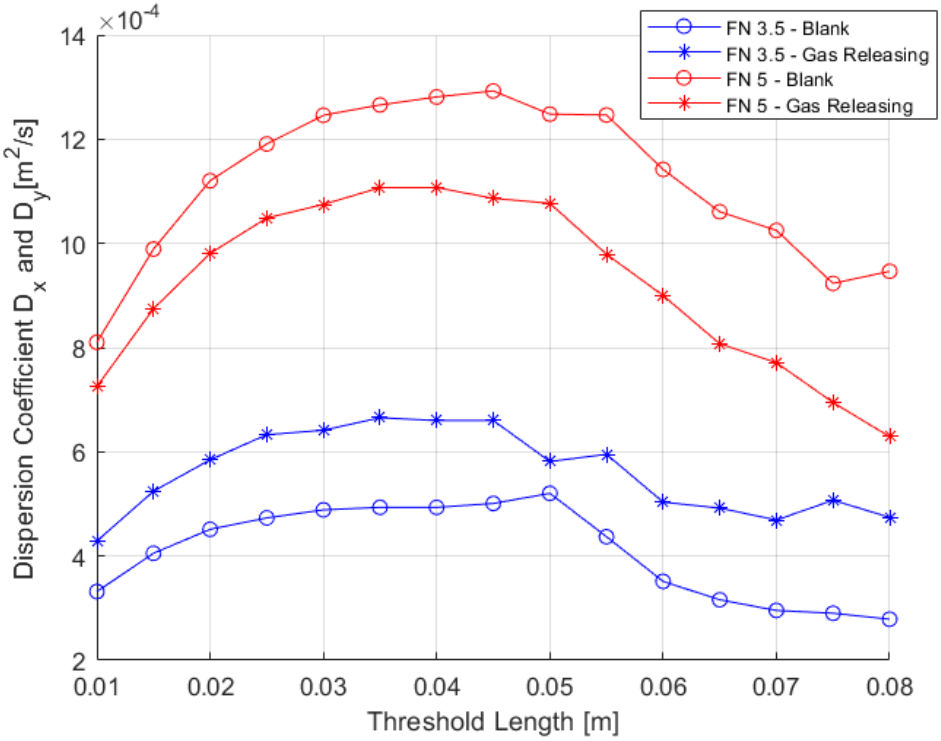

Figure 4.4: Impact of threshold length on dispersion coefficients of high-density tracers at FNs of 3.5 and 5.

Table 4.1 compares the dispersion coefficients for two types of tracers with different densities under varying conditions. The dispersion coefficients are selected from the data in Figures 4.2 and 4.4 when they reach a relatively stable value. At FN = 5, the low-density gas-releasing tracer exhibits a higher coefficient compared to the high-density gas-releasing tracer. This difference is primarily due to the lateral displacement caused by bubble eruptions at the bed surface. For the low-density tracer, which is very light, bubble eruptions easily push them towards the near-wall region, resulting in a higher dispersion coefficient. Conversely, the high-density tracer remains mostly submerged under the bed surface, experiencing less lateral displacement from bubble eruptions.

However, at FN = 3.5, the results are opposite, indicating that the high-density gas-releasing tracer has a higher coefficient than the low-density gas-releasing tracer, which necessitates further investigation.

Table 4.1: Dispersion coefficients (D_x and D_y) under different conditions, $\times 10^{-3}$ m^2/s

	FN = 3.5		**FN = 5**	
Tracer type	**Gas-releasing**	**Blank**	**Gas-releasing**	**Blank**
Low-density tracer	0.4	0.4	1.4	1.1
High-density tracer	0.65	0.5	1.1	1.3

4.2 Axial mixing

4.2.1 Low-density particle

Figure 4.5 illustrates the impact of FNs on the axial position distribution of low-density tracers. At low FNs (FN $\leq$ 2), the position distribution is relatively concentrated, exhibiting high probability density peaks. Particularly at FN = 2, the peak reaches its maximum value, indicating a lower degree of axial mixing. By comparing the axial position with the bed height, it is evident that at low fluidization velocities, the tracers exhibit a strong floating behavior. As the FN gradually increases to 5, the axial distribution of the tracers becomes broader, indicating improved axial mixing. This improvement is attributed to the increased gas flow rate, which results in larger bubble sizes and consequently better mixing within the bed. Additionally, as the fluidization velocity increases, the peak positions shift to the right, which is due to bed expansion compared with low FNs. The increased height of the bed surface allows the tracers to move within a higher axial range. The minimal peak position difference between FN = 3.5 and FN = 5 suggests that the fluidized bed is approaching or has reached a fully fluidized state. In this state, the interaction between the gas and solid phases reaches a dynamic equilibrium, leading to a stabilized axial distribution of particles.

At lower fluidization velocities (FN $\leq$ 2), the gas-releasing tracers penetrate deeper into the dense bed compared to the blank tracers. Conversely, at higher fluidization velocities (FN $\geq$ 3.5), the gas-releasing tracers exhibit axial distribution shifted more to the right (higher positions) than that of the blank tracers. The floating behavior at low FNs can be attributed to the low density of tracer compared to the relatively dense bed, which has relatively low voidage at low FNs. Additionally, the comparatively smaller bubbles do not achieve the immersion of the tracer. As a result, the tracer floats on the bed surface without forming endogenous bubbles. The immersed position could be due to the addition of dry ice, making the tracer heavier, or it might be due to the interaction between the released gas and the bed material. Further investigation is needed. The deeper penetration of the gas-releasing tracers at high FNs could be due to the loosening of the bed by the effect of the gas released. The increased action of bubbles drags the tracer deeper into the bed, where the release of gas might be more likely to promote the formation of endogenous bubbles. These bubbles enhance the buoyancy experienced by the gas-releasing tracer, causing it to occupy a higher axial position within the bed.

Additionally, as the fluidization velocity increases, the distribution differences between gas-releasing tracers and blank tracers gradually diminish. The turbulence intensity significantly increases, forming bubble flows that dominate the fluid dynamics of the bed. These strong turbulence and bubble flows are sufficient to agitate and evenly distribute the particles within the bed, thereby reducing the impact of gas release on the movement of the tracers.

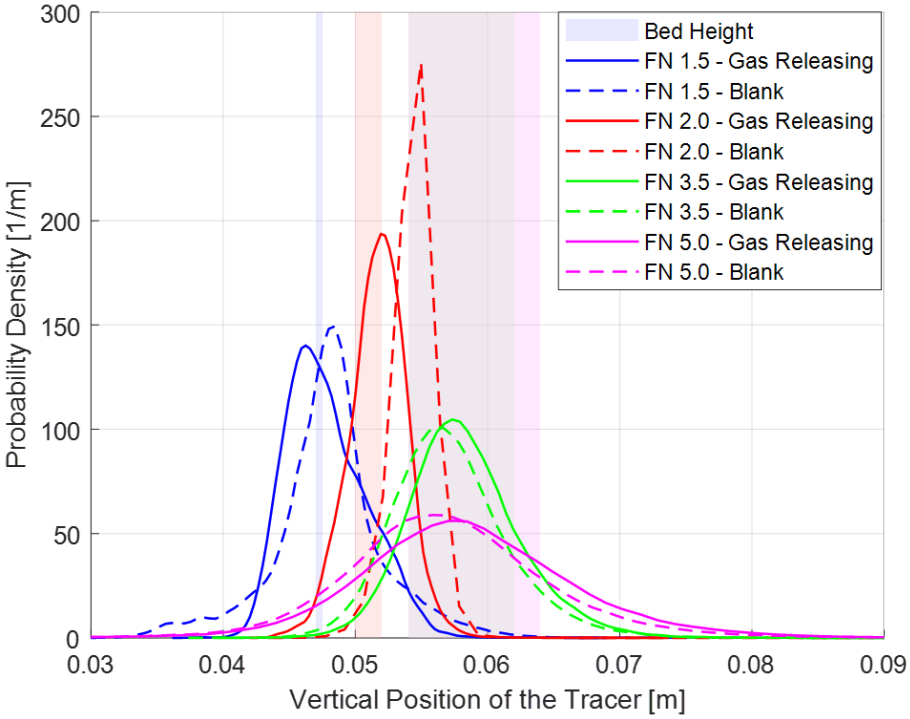

Figure 4.5: Probability density function of the axial location of the low-density tracers for different FNs

To further understand the impact of gas release on axial mixing, the average axial position of the tracers is correlated with the carbon dioxide release rate, as shown in Figure 4.6. With an increase in gas release rate, the positions of the tracers under different FNs exhibit varying degrees of fluctuation. The gas release rate has some influence on the axial position of the tracers, but the specific pattern varies with different FNs. It should be noted that during the experiment, the release rate of carbon dioxide peaks within a very short time (approximately 15 seconds) and then declines steadily while continuously fluctuating. Therefore, when analyzing the behavior of the tracer over time, the analysis should follow the trend from the higher release rate to the lower release rate. This means analyzing the graph from right to left. It is also important to note that there are fewer data points at higher release rates, which may introduce non-robust measurement data.

For low fluidization velocities (FN $\leq$ 2), the movement patterns of the tracers are similar, with minor movements mainly occurring in the corners of the bed surface. However, under FN = 1.5 conditions, the axial position of the tracers fluctuates significantly with the gas release rate, showing strong disturbances, although the reason for this is unclear. Under FN = 2 conditions, the axial distribution of the gas-releasing tracer is more stable. Analyzing the change in the tracer's axial position over time (from high release rates to low release rates) reveals a sinking trend in the tracer's axial position. The position is lower than the average axial position of the blank tracer, which is consistent with previous results indicating that gas release causes the low-density tracer to immerse further down in the bed. When the gas

release rate decreases to approximately 0.25 cm^3/s, the behavior of the gas-releasing tracer becomes more similar to that of the blank tracer. An upward trend in its axial position is observed, further validating the previous conclusion.

For high fluidization velocities (FN $\geq$ 3.5), the fluctuation pattern of the tracers' axial position with changing gas release rates is quite similar, and the amplitude of axial position fluctuations increases with higher release rates. Therefore, under high fluidization number conditions, larger gas release rates have a more significant impact on the internal mixing effect, resulting in a more dynamic and unstable axial distribution of the tracers.

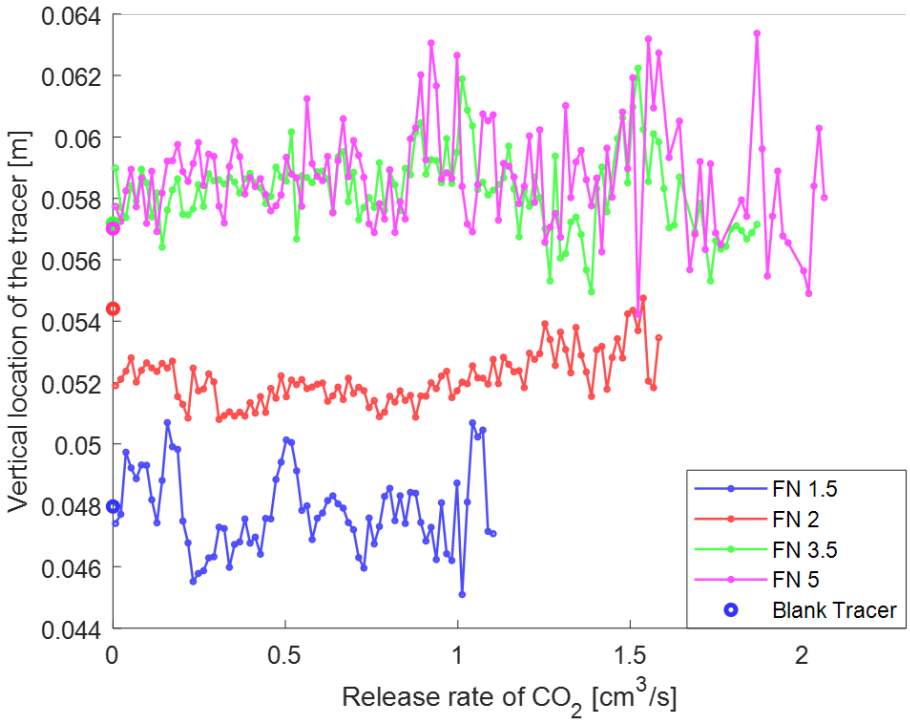

Figure 4.6: Axial position of low-density tracers as a function of the release rate of CO_2.

4.2.2 High-density particle

Figure 14 shows the probability density distribution of the axial position for high-density tracers under different FNs. Due to their high density, tracers consistently sink into the bed. At a FN of 1.5, the axial distribution of the tracers is relatively concentrated at the bottom of the bed. However, for the gas-releasing tracer, an additional peak is observed close to the bed surface. This can be attributed to the gas release causing the tracer to reach higher positions. When FN is 2, both the gas-releasing tracer and the blank tracer exhibit two peaks, near the bottom plate and near the bed surface, with the gas-releasing tracer showing a higher peak value at the elevated position. This suggests that the tracers tend to occupy two axial positions, with the gas-releasing tracer preferring the higher position. Notably, the

higher position closely corresponds to the position of the new peak observed at FN = 1.5.

At FNs of 3.5 and 5, the axial distribution of both gas-releasing and blank tracers becomes more uniform, and the density curves tend to flatten. However, it is still evident that each tracer exhibits two peaks, maintaining the same trend observed at lower fluidization velocity. At higher FNs, the tracers seem to move more intensively in the axial direction, which may be connected to the resulting large lateral dispersion coefficients observed for the bronze tracers at these conditions. Further exploration of these relationships is required.

In summary, the effect of gas release on the axial distribution of tracers is more significant under low fluidization number conditions, especially at FN = 2, and this effect gradually weakens as the FN increases.

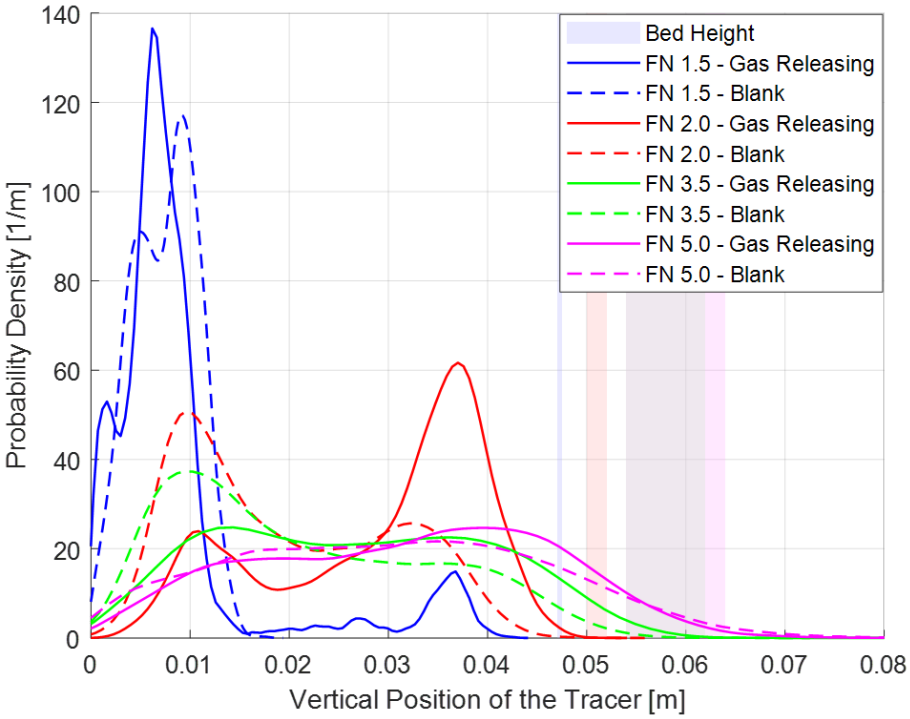

Figure 4.7: Probability density function of the axial location of high-density tracers for different FNs.

The relationship between the average axial position of tracers and the CO_2 release rate is displayed in Figure 4.8. For FN = 1.5, the axial position of the gas-releasing tracer initially rises over time (reading the plot from right to left), likely due to the increased buoyancy caused by high gas release rates, which is also consistent with the new peak observed in the PDF analysis. As the release rate decreases, the axial position significantly drops, suggesting gravity's dominance. At FN = 2, the tracer position in the bed gradually rises over time, attributed to the enhanced buoyancy from endogenous bubbles created by the gas release. However, the mechanism is not

fully understood, as it is unexpected that the tracer tends to remain close to the surface for low gas release rates.

At higher fluidization velocities (FN $\geq$ 3.5), the axial position of the tracers remains relatively stable at lower CO_2 release rates, fluctuating around 0.03 m. When the release rate increases to about 1 cm^3/s, the position of the tracers exhibits significant fluctuations. At high FNs and high CO_2 release rates, the mixing and turbulence effects within the fluidized bed are significantly enhanced.

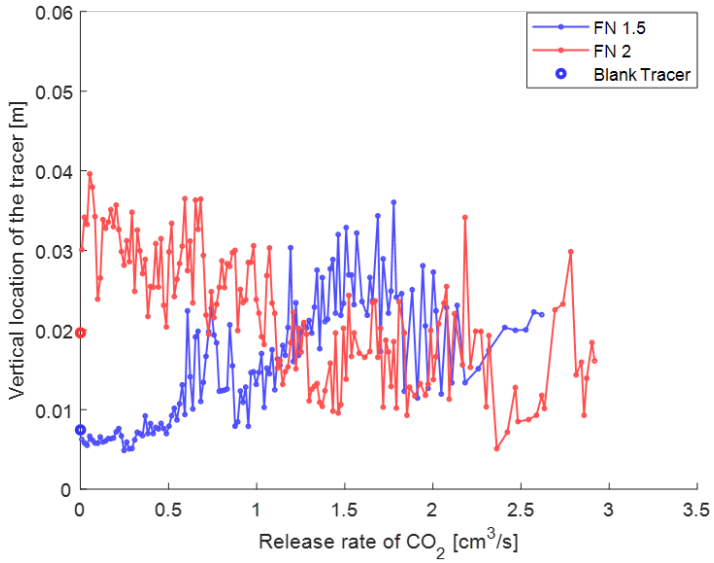

(a) Weak fluidization condition (FN $\leq$ 2).

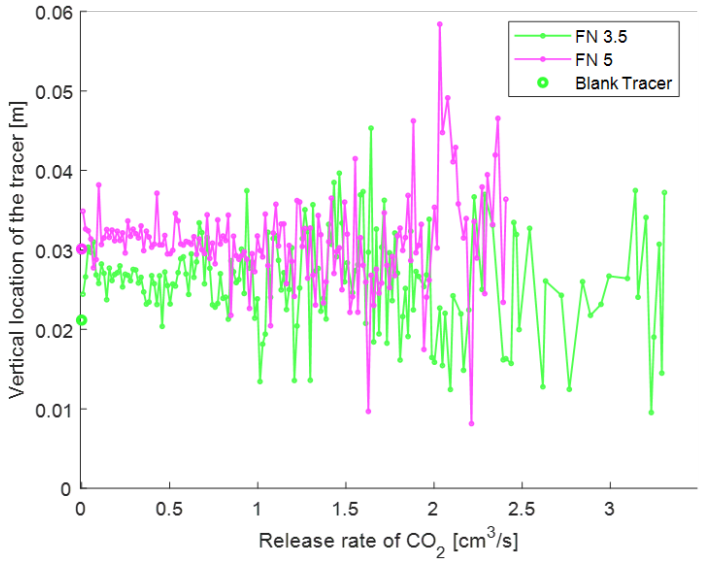

(b) Strong fluidization condition (FN $\geq$ 3.5).

Figure 4.8: Axial position of high-density tracers as a function of the release rate of CO_2.

4.3 Velocity

Since the velocity exhibits very similar changes along the x, y, and z axes, this section discusses only the axial velocity of the low-density tracer for reference. At low FNs (FN $\leq$ 2), the velocity distributions of both the gas-releasing tracers and the blank tracers are highly concentrated around zero (as shown in Figure 4.9). The axial movement of the tracers is minimal, accompanied by a very low axial velocity. When the FN increases to 3.5 and 5, the velocity distribution widens significantly and becomes flatter. This can be attributed to more momentum exchange between the tracer, the bed material, and the bubbles. Factors such as higher bubble frequency, larger bubble size, and more frequent collisions between the tracer and bed material likely contribute to this change. Notably, the differences in velocity distribution between gas-releasing tracers and blank tracers remain negligible.

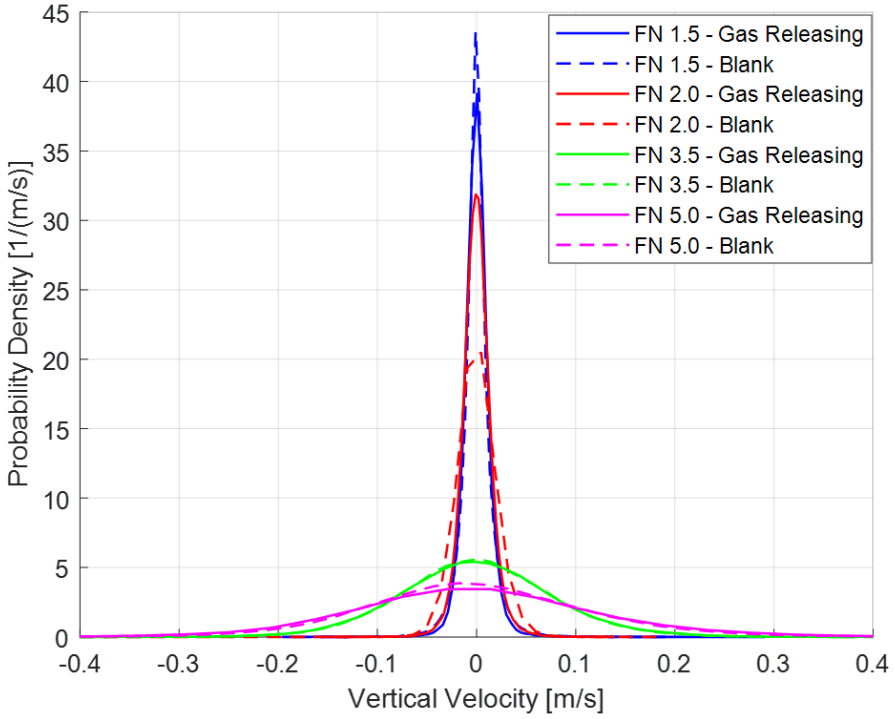

Figure 4.9: Probability density function of the axial velocity of the low-density tracers for different FNs.

Figure 4.10 compares the changes in axial velocity of low-density tracers with varying CO_2 release rates. At low FNs, the axial velocity of the tracers remains generally close to zero with minimal fluctuations at low release rates. As the release rate increases to around 0.8 cm^3/s, the axial velocity of the tracers begins to show some fluctuations, although the amplitude still remains small. Under higher FNs, the axial velocity of the tracers exhibits more significant variations. When the release rate increases to about 0.6 cm^3/s, the axial velocity fluctuations of the tracers intensify, particularly at an FN of 5. The abrupt change in velocity fluctuations may be due to a sudden shift in the force balance acting on the tracer at this specific release

rate.

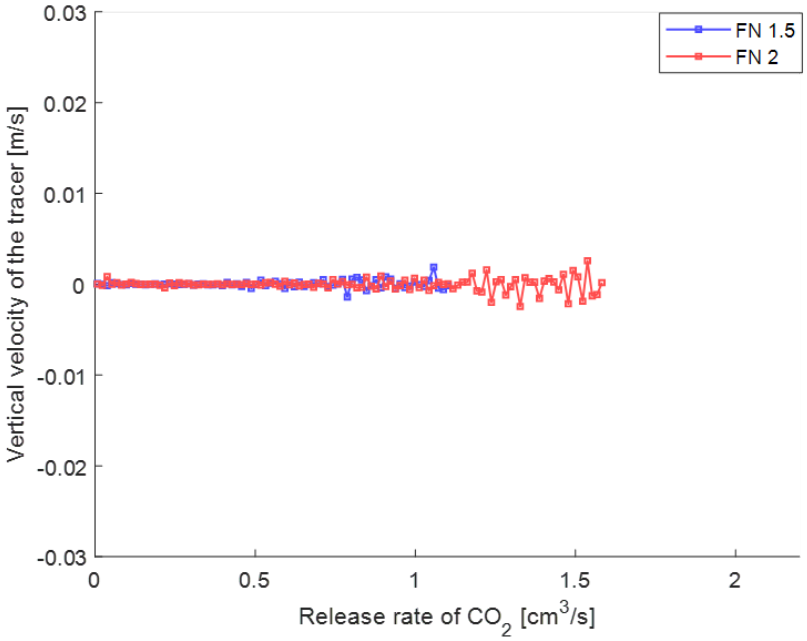

(a) Weak fluidization condition (FN $\leq$ 2.)

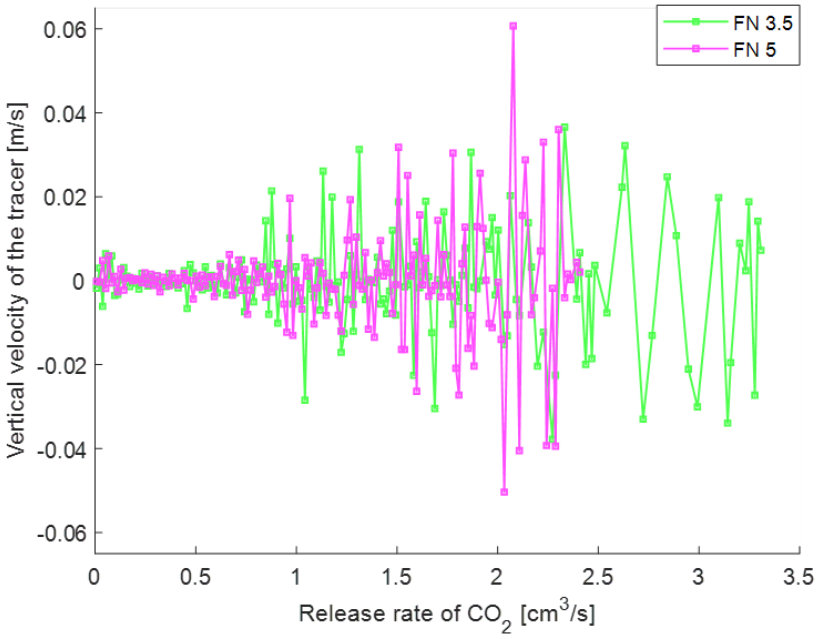

(b) Strong fluidization condition (FN $\geq$ 3.5.)

Figure 4.10: Axial velocity of low-density tracers as a function of the release rate of CO_2.

The axial velocity PDF of the high-density tracers (as shown in Figure A.2 and A.3) is very similar to that of the low-density tracers and is therefore not presented here. The primary difference is that an increase in the gas release rate leads to a larger

variation in the velocity of the high-density tracer. Significant velocity fluctuations occur at gas release rates of approximately 1.4 cm^3/s for low FNs and around 0.75 cm^3/s for high FNs. The higher release rate at which this abrupt change occurs may be attributed to the high-density tracer requiring greater force to overcome gravity.

5
Conclusion

This study utilized three-dimensional Magnetic Particle Tracking technology to track and analyze the trajectories of tracers in a bubbling fluidized bed, primarily investigating the impact of gas release on the mixing of such solids within the bed. Variations of the FN and tracer density were considered in the study.

This study demonstrates that gas release can enhance lateral solids mixing within a bubbling fluidized bed. For low-density tracers, gas release markedly enhances lateral mixing at FN = 5, while the effect is negligible at FN = 3.5. In contrast, for high-density tracers, gas release improves lateral mixing at FN = 3.5 but results in reduced mixing efficiency compared to blank tracers at FN = 5.

For axial mixing, gas release causes low-density tracers to immerse more deeply in the bed at lower FNs (FN $\leq$ 2) but encounter increased buoyancy at higher FNs (FN $\geq$ 3.5), leading to varied positional stability. Besides, gas release promotes high-density tracers to stay at higher positions.

The impact of gas release on velocity is minimal. When the gas release rate reaches a certain value (that depends on the particle density), a clear change is seen in the dispersion of the velocity values, suggesting that the force balance on the tracer is affected.

The present study has relatively fewer data points at high gas release rates, which may affect the statistical robustness of the results. Therefore, future experiments could consider strategies to achieve higher gas release rates, such as using more permeable and porous filler materials in the caps or attempting to load more dry ice within the tracer.

Previous studies suggest that endogenous bubbles formed by gas release are the main cause of increased buoyancy acting on the tracer. This study could not determine whether endogenous bubbles were formed during the experiments. Therefore, future research could focus on visualizing endogenous bubbles concurrently with trajectory tracking.

Bibliography

[1] A. K. Vuppaladadiyam et al., 'A critical review on biomass pyrolysis: Reaction mechanisms, process modeling and potential challenges', Journal of the Energy Institute, vol. 108, p. 101236, Jun. 2023, doi: 10.1016/j.joei.2023.101236.

[2] X. Hu and M. Gholizadeh, 'Biomass pyrolysis: A review of the process development and challenges from initial researches up to the commercialisation stage', Journal of Energy Chemistry, vol. 39, pp. 109–143, Dec. 2019, doi: 10.1016/j.jechem.2019.01.024.

[3] M. Raza et al., 'Progress of the Pyrolyzer Reactors and Advanced Technologies for Biomass Pyrolysis Processing', Sustainability, vol. 13, no. 19, 2021, doi: 10.3390/su131911061.

[4] M. N. Uddin et al., 'An Overview of Recent Developments in Biomass Pyrolysis Technologies', Energies, vol. 11, no. 11, 2018, doi: 10.3390/en11113115.

[5] A. V. Bridgwater, 'Renewable fuels and chemicals by thermal processing of biomass', Chemical Engineering Journal, vol. 91, no. 2, pp. 87–102, Mar. 2003, doi: 10.1016/S1385-8947(02)00142-0.

[6] P. Basu, Biomass Gasification and Pyrolysis: Practical Design and Theory. Elsevier Science, 2010. [Online]. Available: https://books.google.se/books?id=QSypbUSdkikC

[7] A. V. Bridgwater, 'Renewable fuels and chemicals by thermal processing of biomass', Chemical Engineering Journal, vol. 91, no. 2, pp. 87–102, Mar. 2003, doi: 10.1016/S1385-8947(02)00142-0.

[8] A. Köhler, D. Pallarès, and F. Johnsson, 'Magnetic tracking of a fuel particle in a fluid-dynamically down-scaled fluidised bed', Fuel Processing Technology, vol. 162, pp. 147–156, Jul. 2017, doi: 10.1016/j.fuproc.2017.03.018.

[9] S. Iannello, Z. Bond, A. Sebastiani, M. Errigo, and M. Materazzi, 'Axial segregation behaviour of a reacting biomass particle in fluidized bed reactors: experimental results and model validation', Fuel, vol. 338, p. 127234, Apr. 2023, doi: 10.1016/j.fuel.2022.127234.

[10] E. Sette, D. Pallarès, F. Johnsson, F. Ahrentorp, A. Ericsson, and C. Johansson, 'Magnetic tracer-particle tracking in a fluid dynamically down-scaled bubbling fluidized bed', Fuel Processing Technology, vol. 138, pp. 368–377, Oct. 2015, doi: 10.1016/j.fuproc.2015.06.016.

[11] J. Olsson, D. Pallarès, and F. Johnsson, 'Lateral fuel dispersion in a large-scale bubbling fluidized bed', Chemical Engineering Science, vol. 74, pp. 148–159, May 2012, doi: 10.1016/j.ces.2012.02.027.

[12] D. Yang, H. Yu, and R. Li, "Heat Transfer in a Fluidized Bed with Immersed Tubes Using Moist Coal Particles," Arabian journal for science and engineering, vol. 43, pp. 2263–2272, Jun. 2017, doi: 10.1007/s13369-017-2680-2.

[13] R. Solimene, A. Marzocchella, and P. Salatino, 'Hydrodynamic interaction between a coarse gas-emitting particle and a gas fluidized bed of finer solids', Powder Technology, vol. 133, no. 1, pp. 79–90, Jul. 2003, doi: 10.1016/S0032-5910(03)00080-9.

[14] Y. Bai and H. Si, 'Experimental study on fluidization, mixing and separation characteristics of binary mixtures of particles in a cold fluidized bed for biomass fast pyrolysis', Chemical Engineering and Processing - Process Intensification, vol. 153, p. 107936, Jul. 2020, doi: 10.1016/j.cep.2020.107936.

[15] M. Sharifzadeh et al., 'The multi-scale challenges of biomass fast pyrolysis and bio-oil upgrading: Review of the state of art and future research directions', Progress in Energy and Combustion Science, vol. 71, pp. 1–80, Mar. 2019, doi: 10.1016/j.pecs.2018.10.006.

[16] Q. Lu, W.-Z. Li, and X.-F. Zhu, 'Overview of fuel properties of biomass fast pyrolysis oils', Energy Conversion and Management, vol. 50, no. 5, pp. 1376–1383, May 2009, doi: 10.1016/j.enconman.2009.01.001.

[17] M. Raza et al., 'Progress of the Pyrolyzer Reactors and Advanced Technologies for Biomass Pyrolysis Processing', Sustainability, vol. 13, no. 19, 2021, doi: 10.3390/su131911061.

[18] A. K. Varma, R. Shankar, and P. Mondal, 'A Review on Pyrolysis of Biomass and the Impacts of Operating Conditions on Product Yield, Quality, and Upgradation', in Recent Advancements in Biofuels and Bioenergy Utilization, Singapore: Springer Singapore, 2018, pp. 227–259. doi: 10.1007/978-981-13-1307-3-10.

[19] T. Kan, V. Strezov, and T. J. Evans, 'Lignocellulosic biomass pyrolysis: A review of product properties and effects of pyrolysis parameters', Renewable and Sustainable Energy Reviews, vol. 57, pp. 1126–1140, May 2016, doi: 10.1016/j.rser.2015.12.185.

[20] D. Kunii and O. Levenspiel, 'CHAPTER 9 - Solid Movement: Mixing, Segregation, and Staging', in Fluidization Engineering (Second Edition), Boston: Butterworth-Heinemann, 1991, pp. 211–235. doi: 10.1016/B978-0-08-050664-7.50015-9.

[21] X. Bi, 'Gas Fluidization Flow Regimes', in Essentials of Fluidization Technology, 2020, pp. 55–74. doi: 10.1002/9783527699483.ch4.

[22] D. Geldart, 'Types of gas fluidization', Powder Technology, vol. 7, no. 5, pp. 285–292, May 1973, doi: 10.1016/0032-5910(73)80037-3.

[23] P. Salatino and R. Solimene, 'Mixing and segregation in fluidized bed thermochemical conversion of biomass', Powder Technology, vol. 316, pp. 29–40, Jul. 2017, doi: 10.1016/j.powtec.2016.11.058.

[24] D. Pallarès and F. Johnsson, 'A novel technique for particle tracking in cold 2-dimensional fluidized beds—simulating fuel dispersion', Chemical Engineering Science, vol. 61, no. 8, pp. 2710–2720, Apr. 2006, doi: 10.1016/j.ces.2005.11.030.

[25] E. Sette, D. Pallarès, and F. Johnsson, 'Experimental quantification of lateral mixing of fuels in fluid-dynamically down-scaled bubbling flu-

idized beds', Applied Energy, vol. 136, pp. 671–681, Dec. 2014, doi: 10.1016/j.apenergy.2014.09.075.

[26] M. Fiorentino, A. Marzocchella, and P. Salatino, 'Segregation of fuel particles and volatile matter during devolatilization in a fluidized bed reactor—I. Model development', Chemical Engineering Science, vol. 52, no. 12, pp. 1893–1908, Jun. 1997, doi: 10.1016/S0009-2509(97)00018-3.

[27] S. Shrestha, B. S. Ali, and M. D. Binti Hamid, 'Cold flow model of dual fluidized bed: A review', Renewable and Sustainable Energy Reviews, vol. 53, pp. 1529–1548, Jan. 2016, doi: 10.1016/j.rser.2015.09.034.

[28] L. R. Glicksman, M. R. Hyre, and P. A. Farrell, 'Dynamic similarity in fluidization', International Journal of Multiphase Flow, vol. 20, pp. 331–386, Aug. 1994, doi: 10.1016/0301-9322(94)90077-9.

[29] A. Einstein, Investigations on the Theory of the Brownian Movement. Courier Corporation, 1956.

[30] D. C. Guío-Pérez, F. Johnsson, and D. Pallarès, 'Experimental investigation of the lateral mixing of large and light particles immersed in a fluidized bed', Fuel, vol. 346, p. 128343, Aug. 2023, doi: 10.1016/j.fuel.2023.128343.

A

Appendix 1

A.1 Temperature

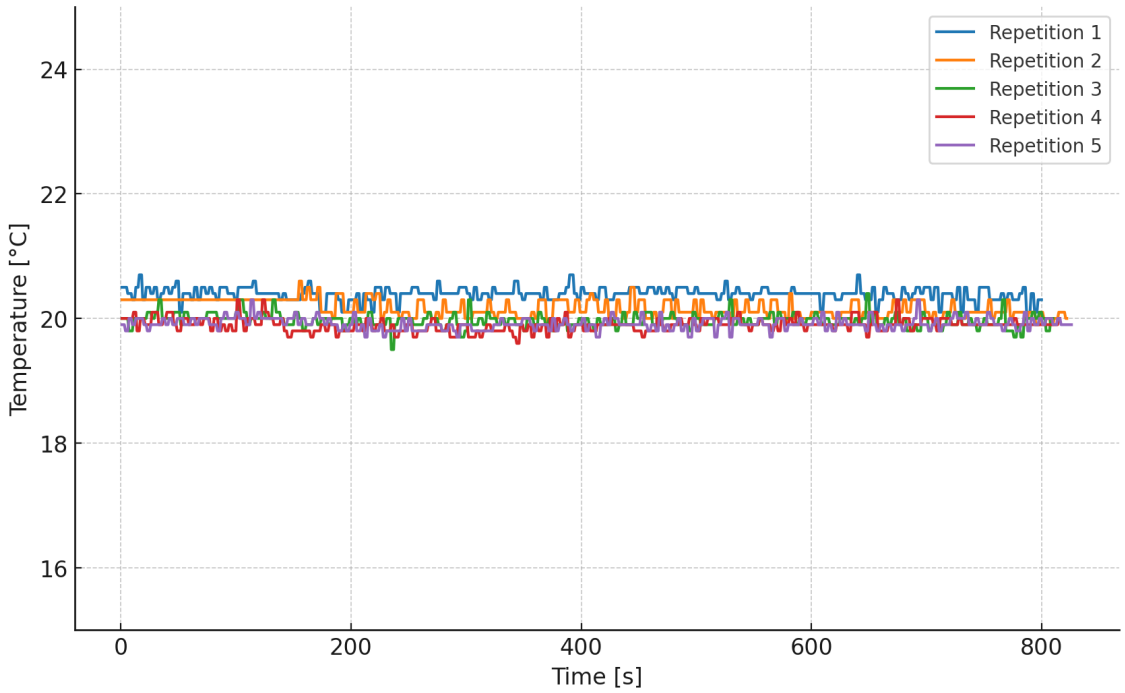

Figure A.1: Temperature variations for five repeated experiments with the high-density tracer at FN = 3.5.

A.2 Axial velocity of high-density tracer

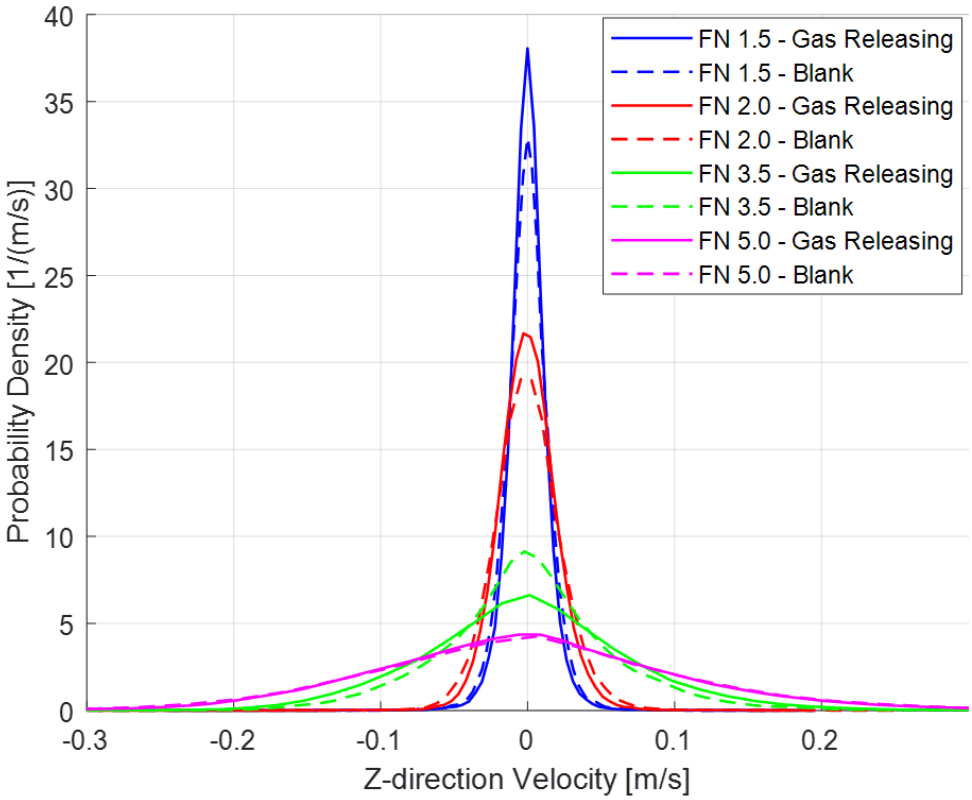

Figure A.2: Probability density function of the axial velocity of the high-density tracers for different FNs.

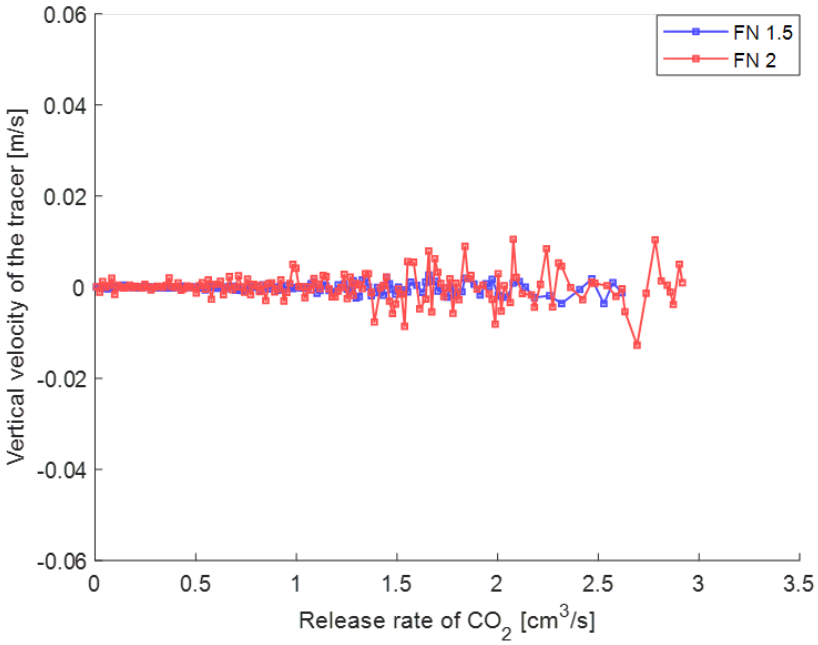

(a) Weak fluidization condition (FN $\leq$ 2.)

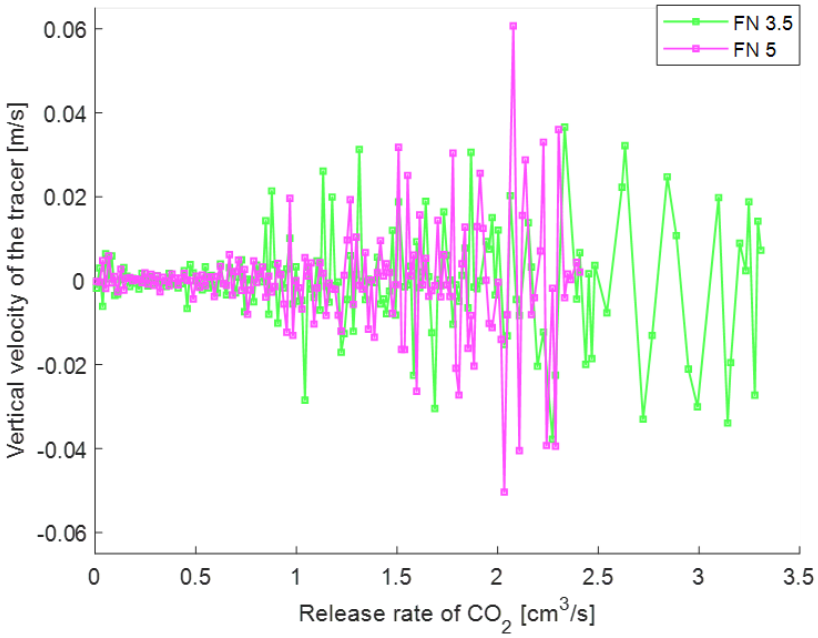

(b) Strong fluidization condition (FN $\geq$ 3.5.)

Figure A.3: Axial velocity of high-density tracers as a function of the release rate of CO_2.

DEPARTMENT OF SPACE, EARTH AND ENVIRONMENT
CHALMERS UNIVERSITY OF TECHNOLOGY
Gothenburg, Sweden
www.chalmers.se

CHALMERS
UNIVERSITY OF TECHNOLOGY